Journal of the Physical Society of Japan **89**, 113702 (2020) **Letters**
https://doi.org/10.7566/JPSJ.89.113702

Non-reciprocal Pumping of Surface Acoustic Waves by Spin Wave Resonance

Kei Yamamoto[1,2*], Weichao Yu[3], Tao Yu[4], Jorge Puebla[2], Mingran Xu[2,5], Sadamichi Maekawa[2,6,1], and Gerrit Bauer[7,3]

[1]*Advanced Science Research Center, Japan Atomic Energy Agency, Tokai, Ibaraki 319-1195, Japan*
[2]*CEMS, RIKEN, Saitama 351-0198, Japan*
[3]*Institute for Materials Research, Tohoku University, Sendai 980-8577, Japan*
[4]*Max Planck Institute for the Structure and Dynamics of Matter, Hamburg 22761, Germany*
[5]*Institute for Solid State Physics, University of Tokyo, Kashiwa, Chiba 277-8581, Japan*
[6]*Kavli Institute for Theoretical Sciences, University of Chinese Academy of Sciences, Beijing 100049, People's Republic of China*
[7]*Advanced Institute for Materials Research, Tohoku University, Sendai 980-8577, Japan*

(Received July 29, 2020; accepted September 16, 2020; published online October 7, 2020)

We predict that surface acoustic waves are generated preferentially in one direction in a heterostructure of a thin magnetic film on a non-magnetic substrate. The non-reciprocity arises from magneto-elastic coupling and magneto-rotation coupling, the former being dominant for YIG/GGG heterostructures. For YIG films thinner than about 100 nm, the surface acoustic wave amplitude is nearly unidirectional at certain angles of the in-plane equilibrium magnetisation. We compute the full magnetic field dependence of the effect for a selected device.

Interactions between spins in magnetic materials and acoustic waves have been attracting much attention in recent years.[1)] Acoustic waves travel much faster and typically possess longer relaxation times than spin waves in the experimentally important GHz frequency range. Moreover, they can be controlled and detected by mechanical forces, and easily converted to electrical signals by piezoelectric substrates. In the context of magnon spintronics, all these features make acoustic waves attractive as signal carriers in insulating materials, motivating a number of studies on the dynamics of elastic deformations in magnetic heterostructures.[2–13)] In particular, Rayleigh-type surface acoustic waves (SAWs) are interesting in their propensity for *chirality* and *non-reciprocity*, where these terms are interpreted as follows: 1. A property or phenomenon is *chiral* if it defines a preferred handedness for three vector quantities. For instance, the Hall effect is chiral since the axes of magnetic field, applied voltage, and Hall current form an either left- or right-handed frame, depending on the sign of Hall coefficient; 2. In a situation where a motion along a reference axis is meaningful, a property or phenomenon is *non-reciprocal* when motions parallel and anti-parallel to the axis are inequivalent. For instance, spin waves under a Dzyaloshinkii–Moriya interaction are non-reciprocal since the eigenfrequency depends linearly on the wave vector.[14)] According to these definitions, the recent experiments[4,6,8,10,12)] indicate that the interaction between magnetisation dynamics and SAWs is chiral, and their transmission across magnetic scatterers is non-reciprocal.

In this letter, we theoretically study the inverse effect to non-reciprocal transmission of SAWs, i.e., the pumping of SAWs by magnetisation dynamics preferentially to left or right depending on the polarisation of the precession direction [Fig. 1(a)]. Specifically, we address the dynamics under ferromagnetic resonance of a thin film of $Y_3Fe_5O_{12}$ (YIG) on a $Gd_3Ga_5O_{12}$ (GGG) substrate [Fig. 1(b)]. Note that the mechanism in Fig. 1(a) also works for a magnetic wire geometry.[15)] Under SAW excitation, atoms near the surface undergo a retrograde rotation[16)] with polarisation locked to the wave vector. Rayleigh SAWs themselves are reciprocal since both senses of rotation are allowed (in contrast to magnetostatic surface spin waves[17)]). However, their coupling with the magnetisation depends on the handedness of the frame formed by the wave vector, the surface normal, and the magnetisation. This implies non-reciprocity in the coupling since the chirality changes sign with the wave vector. We consider this a manifestation of the more general phenomenon of interfacial conversion from angular momentum to linear momentum as depicted in Fig. 2. The inverse Rashba–Edelstein effect,[18,19)] which is a consequence of the spin–orbit interaction in the presence of broken inversion symmetry, affects electrons in an analogous manner. The non-reciprocal SAW generation offers such a conversion

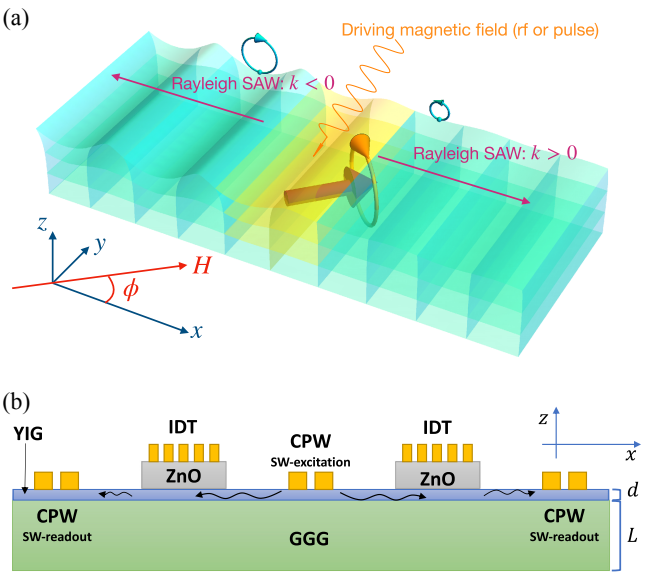

Fig. 1. (Color online) (a) Illustration of the proposed effect. ϕ is the average in-plane magnetisation direction. The ring surrounding the thick arrow at the centre indicates the precessing magnetisation and the other rings at the back represent the rotation of surface atoms. For $0 < \phi < \pi$, energy is dominantly channelled into SAWs propagating in the negative x direction. (b) Schematic of the device considered in this work. Metallic co-planar waveguides (CPW) and piezoelectric crystals (ZnO in this example) with interdigital transducers (IDT) drive and detect spin waves and acoustic waves respectively. L and d are the thickness of the thin magnetic film and the elastic substrate, respectively.

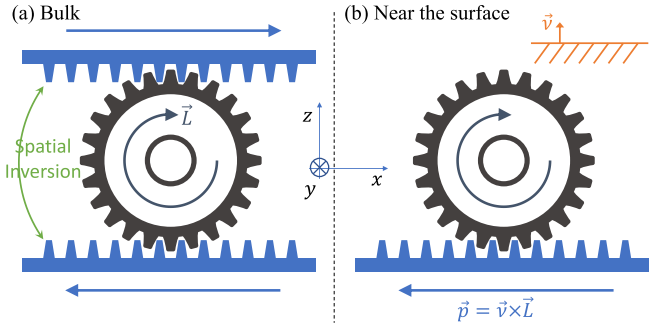

Fig. 2. (Color online) Mechanical analogue of interface conversion from angular momentum to linear momentum. The rotating gears represent angular momentum $\boldsymbol{L}$, while the surfaces with cogs on one side designate surface normals $\boldsymbol{\nu}$. The cogs on the wheel convert the rotation into a linear motion, whose direction is given by the vector product $\boldsymbol{p} = \boldsymbol{\nu} \times \boldsymbol{L}$.

mechanism based on classical wave mechanics (even though the magneto-elastic coupling would vanish without spin–orbit interaction). We derive an analytical formula for the non-reciprocal SAW amplitudes generated by a driving radio-frequency (rf) magnetic field. We show that a unidirectional generation of SAWs is possible at specific angles of the equilibrium magnetisation with respect to the SAW wave vector, at which the SAW is launched exclusively into a single direction.

We consider the magnetisation $\boldsymbol{M}$ of a cubic magnetic material on an isotropic elastic substrate characterised by the displacement vector field $\boldsymbol{u}$. The film normal is along z axis and the magnet fills the region $-d/2 < z < d/2$. In estimating numbers, we take $d = 50\,\mathrm{nm}$, which turns out to optimise the signal strength and non-reciprocity. Let us introduce the normalised dimensionless spin vector $\boldsymbol{n}$ by $\boldsymbol{M} = -M_s \boldsymbol{n}$, where $M_s > 0$ is the saturation magnetisation. We disregard crystalline magnetic anisotropies so that $\boldsymbol{n}, \boldsymbol{u}$ can be taken independent of y without loss of generality as far as plane waves are concerned. In the presence of a static and uniform external field $\boldsymbol{H}$ and an rf magnetic field $\boldsymbol{h}$, the Landau–Lifshitz–Gilbert equation reads

$$\partial_t \boldsymbol{n} = \gamma \mu_0 \boldsymbol{n} \times \left(\boldsymbol{H} + \boldsymbol{h} + \boldsymbol{H}_{\mathrm{eff}} + \boldsymbol{h}_{\mathrm{eff}} - \frac{\alpha}{|\gamma| \mu_0} \partial_t \boldsymbol{n} \right), \tag{1}$$

where $\gamma < 0$ is the gyromagnetic ratio, μ_0 is the permeability of vacuum, α is the Gilbert damping constant, $\boldsymbol{H}_{\mathrm{eff}}$ includes the standard exchange and dipole–dipole interactions,[20] and $\boldsymbol{h}_{\mathrm{eff}}$ is the effective magneto-elastic field. Let $b_{1,2}$ be the cubic magneto-elastic coupling constants in the notation of Ref. 21, and introduce strain and rotation tensors $\epsilon_{ij} = (\partial_j u_i + \partial_i u_j)/2$, $\omega_{ij} = (\partial_j u_i - \partial_i u_j)/2$. Including the magneto-rotation coupling[22,23] originating from the shape anisotropy field, hence proportional to $\mu_0 M_s^2$, we obtain

$$\boldsymbol{h}_{\mathrm{eff}} = \frac{1}{\mu_0 M_s} \begin{pmatrix} 2b_1 \epsilon_{xx} n_x + 2b_2 (\epsilon_{xy} n_y + \epsilon_{xz} n_z) + \mu_0 M_s^2 \omega_{zx} n_z \\ 2b_2 (\epsilon_{yx} n_x + \epsilon_{yz} n_z) + \mu_0 M_s^2 \omega_{zy} n_z \\ 2b_1 \epsilon_{zz} n_z + 2b_2 (\epsilon_{zx} n_x + \epsilon_{zy} n_y) + \mu_0 M_s^2 \omega_{zx} n_x \end{pmatrix}.$$

$\boldsymbol{u}$ obeys the equation of motion

$$\partial_t^2 \boldsymbol{u} = c_S^2 \nabla^2 \boldsymbol{u} + (c_P^2 - c_S^2) \nabla (\nabla \cdot \boldsymbol{u}) + \rho^{-1} (\boldsymbol{f} + \boldsymbol{f}_{\mathrm{eff}}), \tag{2}$$

where ρ is the mass density, $c_{P,S}$ are the longitudinal and transverse sound velocities respectively, and $\boldsymbol{f}$ is an rf external force density generated by the adjacent piezoelectric material such as ZnO, while the effective force density $\boldsymbol{f}_{\mathrm{eff}}$ exerted by the magnetisation dynamics reads

$$\boldsymbol{f}_{\mathrm{eff}} = \partial_x \begin{pmatrix} b_1 n_x^2 \\ b_2 n_x n_y \\ (b_2 + \mu_0 M_s^2/2) n_x n_z \end{pmatrix} + \hat{\partial}_z \begin{pmatrix} (b_2 - \mu_0 M_s^2/2) n_x n_z \\ (b_2 - \mu_0 M_s^2/2) n_y n_z \\ b_1 n_z^2 \end{pmatrix}.$$

We have denoted $\hat{\partial}_z = \partial_z - \delta(z - d/2) + \delta(z + d/2)$ where the delta functions appear as the surface contributions in the derivation based on a variational principle.[24] We ignore the differences in the constitutive parameters $\rho, c_{P,S}$ of the magnet and non-magnet, which is a good approximation for the YIG/GGG combination.

We adopt an external field $\boldsymbol{H} = H(\cos\phi, \sin\phi, 0)$ in the plane and linearise Eq. (1) around the ground state $\boldsymbol{n} \cdot \boldsymbol{H}/H = -1$. Fourier transforms in $t \to \omega$ and $x \to k$ are carried out and the thin film limit ($d^2 \ll |\gamma| A/|\omega| M_s$ with A the exchange stiffness) is taken so that for a given wavenumber k, only one spin wave mode participates in the dynamics. We then expand $\boldsymbol{u}$ in terms of the eigenmodes of Eq. (2) for $\boldsymbol{f}_{\mathrm{eff}} = 0$, i.e., impose free-surface boundary conditions $(c_P^2 - 2c_S^2)\epsilon_{xx} + c_S^2 \epsilon_{zz} = 0$, $\epsilon_{xz} = \epsilon_{yz} = 0$ at $z = d/2$ that give rise to Rayleigh SAW modes and bulk longitudinal and transverse modes.[7,25] When the depth of the elastic body $L \gg d$ is also much greater than c_P/ω, the spin wave coupling to the SAW is larger than that to the bulk modes by a factor of the order $\sqrt{L/d}$, because the surface mode has a much larger overlap with the film than the bulk modes. Restricting ourselves to the vicinity of the band crossing between the Rayleigh mode and spin wave mode, we can safely discard all bulk modes so that $\boldsymbol{u} \approx \sum_k \beta_{R,k} \boldsymbol{v}_{R,k} e^{ikx}$. We chose the SAW mode functions $\boldsymbol{v}_{R,k}$ to be normalised such that $\int_{-L-d/2}^{d/2} |\boldsymbol{v}_{R,k}|^2 \, dz = 1$, which implies the SAW amplitude (per mode) at the top surface is roughly[26] $|\boldsymbol{u}|_{z=d/2} \sim |\beta_{R,k}| \sqrt{|k|L}$. The $|k|L$ dependence is caused by the normalisation and the exponential decay of the surface mode amplitude on the scale $\sim 1/|k|$. We hereafter suppress the k dependence of $\beta_{R,k}$ for brevity. The problem then reduces to

$$\begin{pmatrix} n_\parallel & n_\perp & \beta_R \end{pmatrix}^T = \chi_k(\omega) \begin{pmatrix} h_k^\parallel & h_k^\perp & -f_k \end{pmatrix}^T, \tag{3}$$

where $n_{\parallel,\perp}$ denote the in-plane and out-of-plane components of the spin fluctuation averaged over the film thickness, $h_k^{\parallel,\perp}, f_k$ the Fourier components of the external rf fields, and $\chi_k(\omega)$ the generalised susceptibility given by

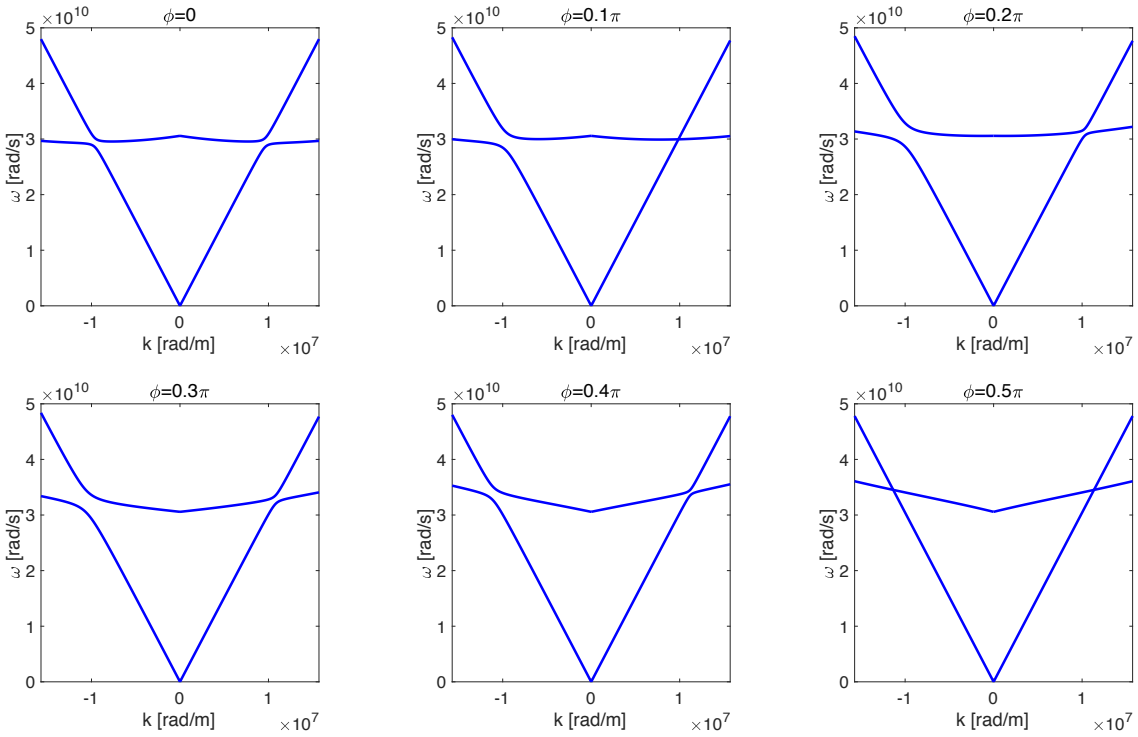

Fig. 3. (Color online) Magnon-polaron dispersion ω_k for selected magnetisation directions ϕ. The parameters are for YIG/GGG heterostructures: $\mu_0 H = 4\pi \times 8.5\,\mathrm{mT}$, $M_s = 1.4 \times 10^5\,\mathrm{A/m}$. $\gamma = -2\pi \times 28 \times 10^9\,\mathrm{rad/(s{\cdot}T)}$, $A = 4\pi \times 5.9 \times 10^{-13}\,\mathrm{J/m}$, $d = 50\,\mathrm{nm}$, $\rho = 7070\,\mathrm{kg/m^3}$, $c_P = 6411\,\mathrm{m/s}$, $c_S = 3568\,\mathrm{m/s}$, $c_R = 3000\,\mathrm{m/s}$, $b_1 = 3.48 \times 10^5\,\mathrm{J/m^3}$, $b_2 = 2b_1$. The exception is $N_R^2 = 3.9 \times 10^{-4}/(|k|L)$, chosen to enhance the anticrossing gap by a factor of 10^3.

$$\chi_k(\omega) = \begin{pmatrix} -H_k^{\parallel} + \dfrac{i\alpha\omega}{\mu_0|\gamma|} & \dfrac{i\omega}{\mu_0|\gamma|} & -\dfrac{1}{\mu_0 M_s} g_{\parallel} \cos\phi \\ -\dfrac{i\omega}{\mu_0|\gamma|} & -H_k^{\perp} + \dfrac{i\alpha\omega}{\mu_0|\gamma|} & -\dfrac{1}{\mu_0 M_s} g_{\perp} \cos\phi \\ -\dfrac{d}{L}\overline{g_{\parallel}} \cos\phi & -\dfrac{d}{L}\overline{g_{\perp}} \cos\phi & \rho\left(\omega^2 - c_R^2 k^2 + \dfrac{i\omega}{\tau}\right) \end{pmatrix}^{-1}.$$

We introduced the sound velocity of the Rayleigh mode c_R, its relaxation time τ, and $H_k^{\parallel} = H + Ak^2/\mu_0 M_s + M_s(1 - N_k)\sin^2\phi$, $H_k^{\perp} = H + Ak^2/\mu_0 M_s + M_s N_k$ with demagnetisation coefficient $N_k = (1 - e^{-|k|d})/|k|d$. The effective coupling constants are

$$g_{\parallel} = -\frac{2ib_1 k}{N_R}(1 - r^2)\{N_{\kappa_P} - (1 - r^2)N_{\kappa_S}\}\sin\phi, \tag{4}$$

$$g_{\perp} = -\frac{\kappa_P}{N_R}\{2b_2(1 - r^2)(N_{\kappa_P} - N_{\kappa_S}) + \mu_0 M_s^2 r^2 N_{\kappa_S}\}, \tag{5}$$

where $N_R \propto 1/\sqrt{|k|L}$ is the SAW normalisation constant [$N_R^2 \approx 0.39/(|k|L)$ for YIG/GGG], $\kappa_{P,S} = |k|\sqrt{1 - c_R^2/c_{P,S}^2}$ denote SAW decay constants, and $r^2 = c_R^2/2c_S^2 \lesssim 1/2$ is a numerical constant. Overbars denote complex conjugation. Crucially, $g_{\parallel}$ is imaginary and odd in k, ϕ while $g_{\perp}$ is real and even.

Let us first examine the hybridisation of the spin wave and SAW, i.e., the dispersion relation of magnon-polarons[27] (Fig. 3) defined as the poles of $\det\chi_k(\omega) = 0$ for vanishing damping $\alpha = 1/\tau = 0$. The hybridisation turns out to be very different for $k > 0$ and $k < 0$, which arises from linear k dependence of $g_{\parallel}$, Eq. (4). The level repulsion between the right-moving spin wave and the SAW with $k > 0$ vanishes at $\phi \approx 0.1\pi$. The level repulsion also disappears at $\phi = \pi/2$ simply because both $g_{\parallel,\perp}$ are accompanied by a factor of $\cos\phi$ in $\chi_k(\omega)$. Figure 3 demonstrates the chiral nature of the magnon-SAW interaction for an unphysically small value of N_R that improves the visibility of the hybridisation.[28] Although the chirality and vanishing of the coupling for the right-mover at $\phi \approx 0.1\pi$ are qualitatively the same for real-world value of N_R, the absolute value of the gap is too small to be presented in graphs. The non-reciprocity is observable when the broadening is smaller than the gap, irrespective of its absolute value.

The hybridisation is so small because $g_{\parallel,\perp}$ are only of the order of MHz at mode frequencies in the GHz range. Nevertheless, the same small coupling can lead to strong mutual conversion between magnons and phonons by a resonant amplification effect.[9,12] We now demonstrate how the magnon-polaron resonance enhances the signal in a pumping experiment in which a spin wave mode is driven by an rf magnetic field. Setting the external mechanical forces $f_k = 0$ for this purpose, the SAW amplitude from Eq. (3) reduces to

$$\beta_R = \frac{d\det\chi_k(\omega)}{L}\left[\left\{\frac{i\omega}{\mu_0|\gamma|}\overline{g_{\perp}} - \left(H_k^{\perp} - \frac{i\alpha\omega}{\mu_0|\gamma|}\right)\overline{g_{\parallel}}\right\}h_k^{\parallel} - \left\{\frac{i\omega}{\mu_0|\gamma|}\overline{g_{\parallel}} + \left(H_k^{\parallel} - \frac{i\alpha\omega}{\mu_0|\gamma|}\right)\overline{g_{\perp}}\right\}h_k^{\perp}\right]\cos\phi. \tag{6}$$

The magnon-polaron hybridisation is broadened by $\alpha, 1/\tau$ so that $\det\chi_k(\omega) \approx -(\omega^2 - c_R^2 k^2 + i\omega/\tau)^{-1} \times (\omega^2 - \omega_k^2 +$

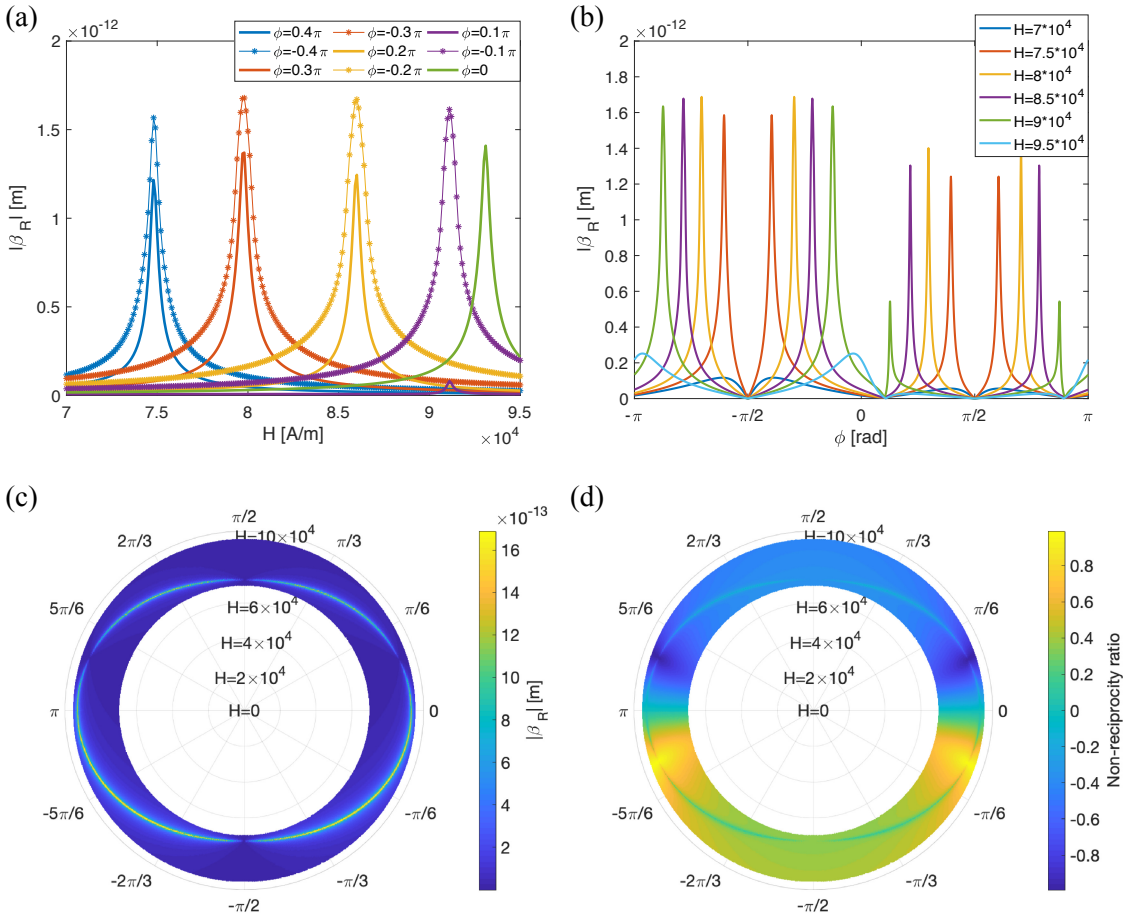

Fig. 4. (Color online) The amplitude of SAW generated by an out-of-plane rf magnetic field (integrated over $k > 0$). We set $h_k^{\perp} = 1$ independent of k for $|k| < k_0$ and zero otherwise. The parameters are chosen $\alpha = 10^{-3}$, $1/\tau = 10^7$ rad/s, $N_R^2 = 0.39/(|k|L)$, and otherwise as in Fig. 3. (a) Field scan at selected angles ($\phi = 0, \pm 0.1\pi, \pm 0.2\pi, \pm 0.3\pi, \pm 0.4\pi$). (b) Angular scan for selected values of $H \in [7 \times 10^4, 9.5 \times 10^4]$. (c) Polar intensity plot of the magnetic field dependence of the SAW amplitude, where $H \in [7 \times 10^4, 9.5 \times 10^4]$ is taken the radial axis. The bright high intensity ring corresponds to the double resonance. (d) Non-reciprocity ratio defined by $(|\beta_R|_{k>0} - |\beta_R|_{k<0})/(|\beta_R|_{k>0} + |\beta_R|_{k<0})$.

$i\alpha\mu_0|\gamma|(H_k^{\parallel} + H_k^{\perp})\omega)^{-1}(\mu_0\gamma)^{-2}\rho^{-1}$, where $\omega_k = \mu_0|\gamma|\sqrt{H_k^{\parallel}H_k^{\perp}}$ is the bare spin wave resonance frequency. The SAW amplitude shows sharp peaks when ω and k simultaneously satisfy the resonance conditions for both SAW and the spin wave, which corresponds to the band crossings in Fig. 3. Spin pumping experiments commonly fix ω and vary H rather than vice versa. In the experimental setup of Fig. 1(b), the rf field contains a broad range of k values governed by the inverse width of the CPW, so that an accordingly k-integrated value of Eq. (6) is observed. Here we take the real space profile $\boldsymbol{h} \propto \mathrm{sinc}(k_0 x)$ with $k_0 = 2\pi \times 10^7$ rad·m/s, modeling a CPW of the width $\gtrsim$100 nm. The results are qualitatively unchanged as long as $k_0 > \omega/c_R \approx 10^7$, which ensures that the wavenumber resonant at ω is included. Figure 4 shows the total SAW amplitude $|\beta_R|$ for $k > 0$ as a function of H and ϕ for realistic values of the parameters including N_R. We focus on out-of-plane driving fields $h_k^{\parallel} = 0$ since co-planer waveguides tend to have $|h_k^{\perp}| \gg |h_k^{\parallel}|$. Nonzero $h_k^{\parallel}$ turns out not to alter the results qualitatively. Non-reciprocity is clearly seen as an asymmetry between $\phi > 0$ and $\phi < 0$. For the waves propagating in the positive x direction, the signal is larger for $\phi < 0$, as depicted in Fig. 1(a). The resonance line shapes generally have two peaks corresponding to the magnon-polaron level repulsion. However, they are smeared out by the dissipations $\alpha, 1/\tau$ to an asymmetric broadening of the resonance. The broadening is more pronounced for $\phi < 0$ than for $\phi > 0$, which is consistent since a larger effective coupling increases both the peak height and the splitting. Note that even when H and ϕ satisfy the double resonance condition, $|\beta_R|$ is strongly suppressed for $\phi \approx 0.1\pi, 0.9\pi$ for $k > 0$ [Fig. 4(c)]. This is the counterpart of the vanishing level repulsion in the magnon-polaron dispersion. From Eq. (6), we estimate the angles at which the effective coupling vanishes for out-of-plane driving to be at $i\omega\overline{g_{\parallel}}/\mu_0|\gamma| - H_k^{\parallel}\overline{g_{\perp}} \approx 0$, which upon using Eqs. (4) and (5) yields

$$\sin\phi \approx -\frac{|\gamma|\mu_0 H_k^{\parallel}}{\omega}\frac{\kappa_P}{k}\frac{2b_2(N_{\kappa_P} - N_{\kappa_S}) + \mu_0 M_s^2 r^2 N_{\kappa_S}}{2b_1\{N_{\kappa_P} - (1-r^2)N_{\kappa_S}\}}. \quad (7)$$

At the resonance, $\omega = |\gamma|\mu_0\sqrt{H_k^{\perp}H_k^{\parallel}}$ so that the prefactor is of order unity. Noting $\kappa_P/k \sim \mathrm{sgn}(k)$, Eq. (7) has a solution for ϕ whenever b_1 is sufficiently larger than $b_2, \mu_0 M_s^2$. For thin films, $N_{\kappa_S} - N_{\kappa_P} \sim (\kappa_P - \kappa_S)d/2 \ll r^2 N_{\kappa_S} \lesssim 1$, hence there is almost always a solution for ϕ. If the film is very thin $|k|d \ll 1$ and the magneto-rotation coupling is small, i.e., $\mu_0 M_s^2 \ll |b_{1,2}|$, the angle at which the effective coupling vanishes approaches $\phi = 0, \pi$, as observed in Ref. 12. In the YIG film with $\omega/2\pi = 5$ GHz and $d = 50$ nm considered here, $b_1 \gtrsim |b_2(N_{\kappa_P} - N_{\kappa_S})| \gg \mu_0 M_s^2$. Therefore, the effective coupling vanishes at values of ϕ close to $\pm 0.1\pi$, causing a unidirectional generation of SAWs in the proposed device.

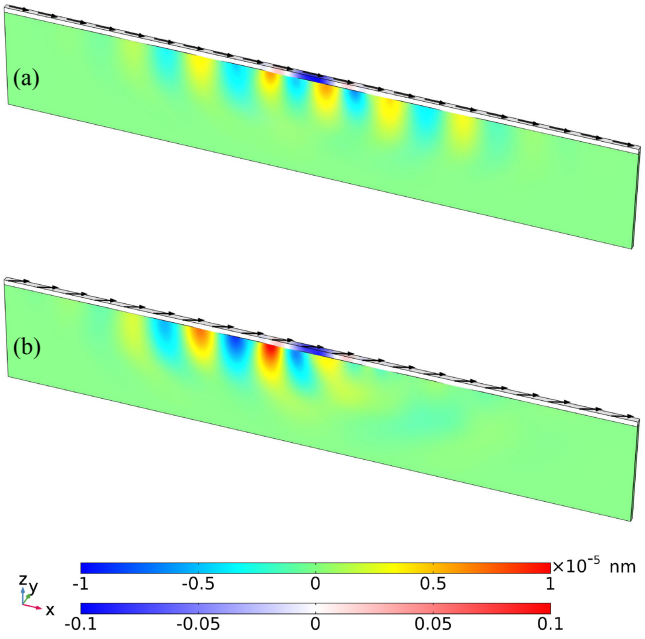

Fig. 5. (Color online) Numerical simulation of the magnetic-elastic hybrid system of a magnetic film (YIG, 50 nm thick) on a substrate (GGG, 1 μm thick). Snapshots of the spin waves and SAW excited by a magnetic field pulse at $t = 1$ ns for different magnetization plotted in black arrows (a) $\phi = 0$ and (b) $\phi = 0.36$. The rainbow colour code indicates u_z and the colour code inside YIG film indicates n_z. While the elastic parameters given in Fig. 3 are used for GGG, we here use realistic values for YIG as well: $\rho^{\mathrm{YIG}} = 5170$ kg/m^3, $c_P^{\mathrm{YIG}} = 7209$ m/s, $c_S^{\mathrm{YIG}} = 3843$ m/s. We suppress wave reflections at the edges by attaching regions with large damping parameters.

To corroborate the analytical calculations, we solve the coupled Eqs. (1) and (2) numerically using COMSOL based on finite elements method.[29] This serves the purpose of justifying two simplifying assumptions above, viz. treating the GGG and YIG as a single uniform elastic body, and discarding all but one spin and one acoustic wave mode. In the numerical simulation, we consider only exchange interaction in the YIG film and approximate the dipolar field as a hard-axis anisotropy $H_{\mathrm{ani}}^{\mathrm{eff}} = -M_s n_z \hat{\mathbf{e}}_z$. With a static in-plane field $H = 8.8 \times 10^4$ A/m, the Kittel mode of the film is at $f_0 = \gamma\sqrt{H(H+M_s)}/2\pi = 5$ GHz. An rf driving magnetic field $[\boldsymbol{h} = a\sin(2\pi f_0 t)\hat{\mathbf{e}}_z]$ with magnitude $a = 10$ mT is applied to the central region of the YIG film (width 50 nm). Spin waves are excited and converted into SAW due to the magneto-elastic coupling. As shown in Fig. 5, the SAWs are launched equally into both directions for $\phi = 0$, consistent with the prediction in Ref. 11. For $\phi = 0.36$, the SAW propagates preferentially along $-\hat{\boldsymbol{x}}$. The non-vanishing signals in the $+\hat{\boldsymbol{x}}$ direction are bulk acoustic waves resonant at 5 GHz, which we disregarded in the analytics.

In conclusion, we theoretically established that reciprocal spin waves couple non-reciprocally to Rayleigh SAWs and the resonance between them pumps SAWs preferentially in a single direction. The proposed effect can be considered a phonon counterpart of the inverse Rashba–Edelstein effect from symmetry perspectives. It is notable that the smallness of the spin–orbit interaction that underlies the magneto-acoustic couplings, can be compensated by a resonant amplification. This leads to a substantial non-reciprocity[12] and the unidirectional pumping of SAWs predicted here. The experimental observation of the latter would be an important step forward in the pursuit of insulator-based computational devices.

Acknowledgments The authors would like to thank Kazuya Harii, Jun'ichi Ieda, Hidekazu Kurebayashi, and Michiyasu Mori for helpful comments. This work was performed under the Inter-University Cooperative Research Program of the Institute for Materials Research, Tohoku University (Proposal Nos. 19K0007, 20K0033), and was supported by JSPS KAKENHI Grant Numbers JP19K21040, JP20K14369, JP20237075, JP19J21720, JP19H006450, JP20H01865.

*yamamoto.kei@jaea.go.jp

1) J. Puebla, M. Xu, B. Rana, K. Yamamoto, S. Maekawa, and Y. Otani, J. Phys. D **53**, 264002 (2020).
2) M. Weiler, L. Dreher, C. Heeg, H. Huebl, R. Gross, M. S. Brandt, and S. T. B. Goennenwein, Phys. Rev. Lett. **106**, 117601 (2011).
3) M. Weiler, H. Huebl, F. S. Goerg, F. D. Czeschka, R. Gross, and S. T. B. Goennenwein, Phys. Rev. Lett. **108**, 176601 (2012).
4) R. Sasaki, Y. Nii, Y. Iguchi, and Y. Onose, Phys. Rev. B **95**, 020407 (2017).
5) D. Kobayashi, T. Yoshikawa, M. Matsuo, R. Iguchi, S. Maekawa, E. Saitoh, and Y. Nozaki, Phys. Rev. Lett. **119**, 077202 (2017).
6) M. Xu, J. Puebla, F. Auvray, B. Rana, K. Kondou, and Y. Otani, Phys. Rev. B **97**, 180301 (2018).
7) R. Verba, I. Lisenkov, I. Krivorotov, V. Tiberkevich, and A. Slavin, Phys. Rev. Appl. **9**, 064014 (2018).
8) A. Hernández-Mínguez, F. Macià, J. M. Hernàndez, J. Herfort, and P. V. Santos, Phys. Rev. Appl. **13**, 044018 (2020).
9) K. An, A. N. Litvinenko, R. Kohno, A. A. Fuad, V. V. Naletov, L. Vila, U. Ebels, G. de Loubens, H. Hurdequint, N. Beaulieu, J. Ben Youssef, N. Vukadinovic, G. E. W. Bauer, A. N. Slavin, V. S. Tiberkevich, and O. Klein, Phys. Rev. B **101**, 060407 (2020).
10) S. Tateno and Y. Nozaki, Phys. Rev. Appl. **13**, 034074 (2020).
11) X. Zhang, G. E. W. Bauer, and T. Yu, Phys. Rev. Lett. **125**, 077203 (2020).
12) M. Xu, K. Yamamoto, J. Puebla, K. Baumgaertl, B. Rana, K. Miura, H. Takahashi, D. Grundler, S. Maekawa, and Y. Otani, Sci. Adv. **6**, eabb1724 (2020).
13) M. Küß, M. Heigl, L. Flacke, A. Hörner, M. Weiler, M. Albrecht, and A. Wixforth, arXiv:2004.03535.
14) J.-h. Moon, S.-m. Seo, K.-J. Lee, K.-w. Kim, J. Ryu, H.-w. Lee, R. D. McMichael, and M. D. Stiles, Phys. Rev. B **88**, 184404 (2013).
15) (Supplemental Materials) The analytical calculations for a magnetic wire on an extended elastic substrate is provided online [Eqs. (S7), (S22), (S23)].
16) W. M. Telford, L. P. Geldart, and R. E. Sheriff, *Applied Geophysics* (Cambridge University Press, New York, 1990) 2nd ed., p. 792.
17) R. Damon and J. Eshbach, J. Phys. Chem. Solids **19**, 308 (1961).
18) J. C. R. Sánchez, L. Vila, G. Desfonds, S. Gambarelli, J. P. Attané, J. M. De Teresa, C. Magén, and A. Fert, Nat. Commun. **4**, 2944 (2013).
19) K. Shen, G. Vignale, and R. Raimondi, Phys. Rev. Lett. **112**, 096601 (2014).
20) D. D. Stancil and A. Prabhakar, *Spin Waves* (Springer, New York, 2009).
21) A. E. Clark, B. DeSavage, W. Coleman, E. R. Callen, and H. B. Callen, J. Appl. Phys. **34**, 1296 (1963).
22) H. F. Tiersten, J. Math. Phys. **5**, 1298 (1964).
23) S. Maekawa and M. Tachiki, AIP Conf. Proc. **29**, 542 (1976).
24) (Supplemental Material) Derivation of the equations of motion from free energies are provided online (Section I).
25) L. D. Landau and E. M. Lifshitz, *Theory of Elasticity* (Butterworth, Oxford, U.K., 1986) Vol. 7, 3rd ed., p. 196.
26) (Supplemental Material) Details of the mode functions and their normalization are provided online (Section II).
27) B. Flebus, K. Shen, T. Kikkawa, K.-i. Uchida, Z. Qiu, E. Saitoh, R. A. Duine, and G. E. W. Bauer, Phys. Rev. B **95**, 144420 (2017).
28) N_R is here just a parameter that tunes the coupling through Eqs. (4) and (5), without a physical meaning.
29) COMSOL Multiphysics® v. 5.4. www.comsol.com. COMSOL AB, Stockholm, Sweden.

Supplemental materials

Kei Yamamoto,[1,2,*] Weichao Yu,[3] Tao Yu,[4] Jorge Puebla,[2] Mingran Xu,[2,5] Sadamichi Maekawa,[2,6,1] and Gerrit Bauer[3,7]

[1]*Advanced Science Research Center, Japan Atomic Energy Agency, Tokai 319-1195, Japan*
[2]*CEMS, RIKEN, Saitama, 351-0198, Japan*
[3]*Institute for Materials Research, Tohoku University, Sendai 980-8577, Japan*
[4]*Max Planck Institute for the Structure and Dynamics of Matter, 22761 Hamburg, Germany*
[5]*Institute for Solid State Physics, University of Tokyo, 5-1-5 Kashiwanoha, Kashiwa, Chiba 277-8581, Japan*
[6]*Kavli Institute for Theoretical Sciences, University of Chinese Academy of Sciences, Beijing 100049, People's Republic of China*
[7]*Advanced Institute for Materials Research, Tohoku University, Sendai 980-8577, Japan*

(Dated: September 17, 2020)

CONTENTS

I. LINEARISATION AND EXTENSION TO WIRE GEOMETRY

We consider a slab of non-magnetic elastic body with thickness L_z and width L_x, on which a slab of ferromagnetic with thickness $d \ll L_z$ and width w is attached. Both are assumed infinitely extended in the y direction and dynamics uniform in y is considered. Our model is based on the phenomenological total free energy $E = W + F + I$ where W, F are the magnetic and elastic energies respectively and I is the interaction energy between $\boldsymbol{M}$ and $\boldsymbol{u}$. We take

$$W = \int d\boldsymbol{r} \left\{ -\mu_0 \boldsymbol{M} \cdot (\boldsymbol{H} + \boldsymbol{h}) - \frac{A}{2} \boldsymbol{n} \cdot \nabla^2 \boldsymbol{n} + \frac{\mu_0 M_s^2}{8\pi} \int d\boldsymbol{r}' \left(\boldsymbol{n} \cdot \nabla\right) \left(\boldsymbol{n}' \cdot \nabla'\right) \frac{1}{|\boldsymbol{r} - \boldsymbol{r}'|} \right\}, \tag{S.1}$$

$$F = \rho \int d\boldsymbol{r} \left\{ \frac{c_P^2 - 2c_S^2}{2} \left(\epsilon_{xx} + \epsilon_{yy} + \epsilon_{zz}\right)^2 + c_S^2 \left(\epsilon_{xx}^2 + \epsilon_{yy}^2 + \epsilon_{zz}^2 + 2\epsilon_{xy}^2 + 2\epsilon_{yz}^2 + 2\epsilon_{zx}^2\right) \right\}, \tag{S.2}$$

$$\begin{aligned} I = \int d\boldsymbol{r} \Big[& b_1 \left(\epsilon_{xx} n_x^2 + \epsilon_{yy} n_y^2 + \epsilon_{zz} n_z^2\right) + 2b_2 \left(\epsilon_{xy} n_x n_y + \epsilon_{yz} n_y n_z + \epsilon_{zx} n_z n_x\right) \\ & + \mu_0 M_s^2 \left\{ (1 - N_\perp) n_x \left(n_z \omega_{zx} + n_y \omega_{yx}\right) + N_\perp n_z \left(n_x \omega_{xz} + n_y \omega_{yz}\right) \right\} \Big], \end{aligned} \tag{S.3}$$

where $N_\perp = w/(w + d)$ is the demagnetising factor of the magnetic slab. In the main text, we focused on the case of an infinite film $L_x = w \to \infty$. Here we also include another limiting case of narrow wire $w \ll L_x$ as the two cases can readily be discussed in parallel (see Fig. S1).

We begin by writing down the linearised version of Eqs. (1) and (2) in the main text, which are derived from the free energy functional above by a variational principle:

$$\begin{pmatrix} -H_\parallel + i\alpha\omega/\mu_0|\gamma| & i\omega/\mu_0\,|\gamma| \\ -i\omega/\mu_0\,|\gamma| & -H_\perp + i\alpha\omega/\mu_0|\gamma| \end{pmatrix} \begin{pmatrix} n_\parallel \\ n_\perp \end{pmatrix} = -\frac{\gamma}{|\gamma|} \left(\boldsymbol{h} + \boldsymbol{h}_{\rm eff}\right), \tag{S.4}$$

$$\rho \left\{ \left(\omega^2 + c_S^2 \nabla^2\right) \boldsymbol{u} + \left(c_P^2 - c_S^2\right) \begin{pmatrix} \partial_x \\ 0 \\ \partial_z \end{pmatrix} (\partial_x u_x + \partial_z u_z) \right\} = -\boldsymbol{f} - \boldsymbol{f}_{\rm eff}, \tag{S.5}$$

* yamamoto.kei@jaea.go.jp

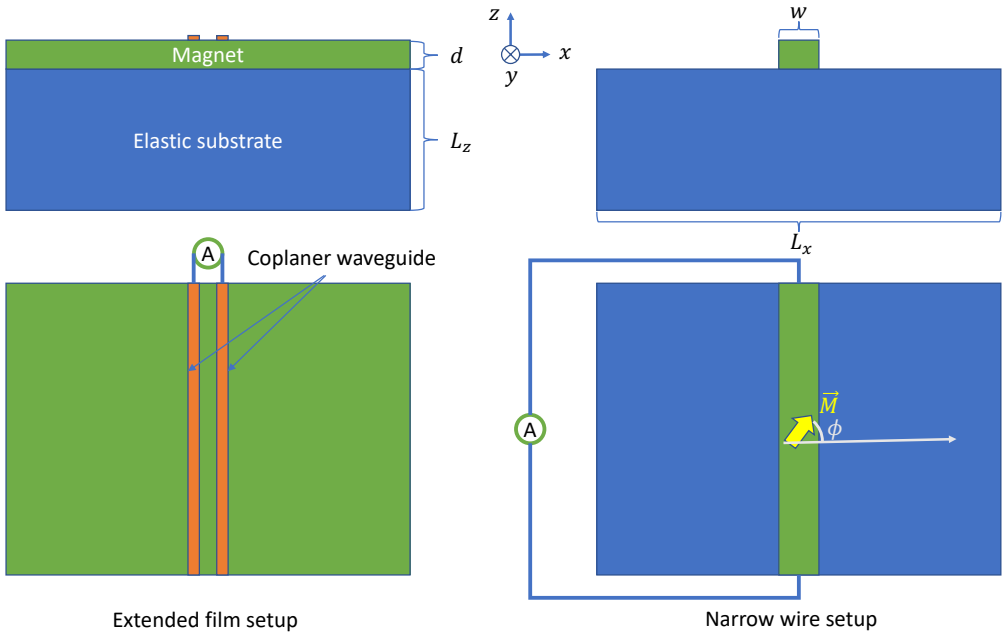

FIG. S1. Schematics of the film geometry (left) and wire geometry (right) considered in the supplementary materials.

where the normalised spin vector $\boldsymbol{n}$ has been expanded as

$$\boldsymbol{n} \approx \begin{pmatrix} \cos\theta \\ \sin\theta \\ 0 \end{pmatrix}\left(1 - \frac{n_\parallel^2 + n_\perp^2}{2}\right) + n_\parallel \begin{pmatrix} -\sin\theta \\ \cos\theta \\ 0 \end{pmatrix} + n_\perp \begin{pmatrix} 0 \\ 0 \\ 1 \end{pmatrix}, \tag{S.6}$$

and the Fourier transform in time has been applied. The internal fields $H_{\parallel,\perp}$ take different forms for the film and wire:

$$H_\parallel = \begin{cases} H - \frac{A}{\mu_0 M_s}\partial_x^2 + M_s\left(1 - N_k\right)\sin^2\theta & \text{film} \\ H\left|\cos\left(\theta - \phi\right)\right| + M_s\left(1 - N_\perp\right)\sin^2\theta & \text{wire} \end{cases}, \quad H_\perp = \begin{cases} H - \frac{A}{\mu_0 M_s}\partial_x^2 + M_s N_k & \text{film} \\ H\left|\cos\left(\theta - \phi\right)\right| + M_s N_\perp & \text{wire} \end{cases}. \tag{S.7}$$

Note $N_\perp = 1$ for film by definition, and for wire in general $\phi \neq \theta$ due to the in-plane shape anisotropy. The linearised effective forces are given by

$$\boldsymbol{h}_{\text{eff}} = -\frac{\gamma/|\gamma|}{\mu_0 M_s}\begin{pmatrix} -2b_1\epsilon_{xx}\cos\phi\sin\phi + \left\{2b_2\epsilon_{xy} - \left(1 - N_\perp\right)\omega_{xy}\right\}\left(\cos^2\phi - \sin^2\phi\right) \\ 2b_2\left(\epsilon_{zx}\cos\phi + \epsilon_{zy}\sin\phi\right) - N_\perp\omega_{zy}\sin\phi - \left(2N_\perp - 1\right)\omega_{zx}\cos\phi \end{pmatrix}, \tag{S.8}$$

$$\boldsymbol{f}_{\text{eff}} = \hat{\partial}_x\begin{pmatrix} -2b_1 n_\parallel\cos\phi\sin\phi \\ \left\{b_2 + \mu_0 M_s^2\left(1 - N_\perp\right)/2\right\} n_\parallel\left(\cos^2\phi - \sin^2\phi\right) \\ \left\{b_2 - \mu_0 M_s^2\left(2N_\perp - 1\right)/2\right\} n_\perp\cos\phi \end{pmatrix} + \hat{\partial}_z\begin{pmatrix} \left\{b_2 + \mu_0 M_s^2\left(2N_\perp - 1\right)/2\right\}\cos\phi \\ \left(b_2 + \mu_0 M_s^2 N_\perp/2\right)\sin\phi \\ 0 \end{pmatrix} n_\perp, \tag{S.9}$$

where $\hat{\partial}_x = \partial_x - \delta\left(x - w/2\right) + \delta\left(x + w/2\right)$. The delta functions in $\boldsymbol{f}_{\text{eff}} = -\delta I/\delta\boldsymbol{u}$ arise from the boundary terms when taking the variation of I with respect to $\boldsymbol{u}$. Therefore, omitting them would lead to non-conservation of energy at the boundaries. Although they could have been regarded as additional boundary conditions, that would have resulted in discussing modifications to the spatial profile of SAWs. As this task appears to be complicated if not intractable, and distracts attentions from the essential physics, we opt for an approximation scheme established in Ref. 6 of the main text.

II. MODE EXPANSION

We expand the full solutions of Eqs. (S.4) and (S.5) in terms of the individual solutions for Eq. (S.4) with $\boldsymbol{h}_{\text{eff}} = 0$ and Eq. (S.5) with $\boldsymbol{f}_{\text{eff}}$. In doing so for $n_{\parallel,\perp}$, we assume the film is sufficiently thin, i.e. $(d/2\pi)^2 < A/\mu_0 M_s^2$, so that the spin wave

modes are quantised along the thickness direction and all but the lowest frequency band may be disregarded. For YIG, the condition translates to roughly $d < 100$ nm. For films, the in-plane wavenumber k is a conserved quantity, which makes it possible to focus on one spin wave mode only in the expansion. For wires, if $w \gg 100$ nm, many spin wave modes with different k have to be retained in the expansion. To avoid this complication, we also assume $w < 100$ nm so that the expansion contains only the Kittel mode.

The expansion of $\boldsymbol{u}$ is common to the film and wire geometries. We impose the free-surface boundary conditions $\left(c_P^2 - 2c_S^2\right)\epsilon_{xx} + c_S^2\epsilon_{zz} = 0, \epsilon_{xz} = \epsilon_{yz} = 0$ at $z = d/2$, while the limit $L_z \to \infty$ is understood in order to ignore the boundary conditions on that surface. L_x is also assumed large so that Fourier transform in x is meaningful. There are four types of modes: a longitudinal mode (primary wave) $\boldsymbol{v}_{P,k,k_z}$ with velocity c_P, two transverse modes (secondary wave) $\boldsymbol{v}_{S,k,k_z}, \boldsymbol{v}_{T,k,k_z}$ with velocity c_S, and one surface (Rayleigh) mode $\boldsymbol{v}_{R,k}$ with velocity c_R. Note that the bulk modes (P,S,T) have the additional label $k_z > 0$ and the surface sound velocity c_R is determined by solving

$$\left(\frac{c_R}{c_S}\right)^3 - 8\left(\frac{c_R}{c_S}\right)^2 + 8\left\{3 - 2\left(\frac{c_S}{c_P}\right)^2\right\}\frac{c_R}{c_S} - 16\left\{1 - \left(\frac{c_S}{c_P}\right)^2\right\} = 0. \tag{S.10}$$

The general deformation $\boldsymbol{u}$ satisfying the free-surface boundary conditions can be expanded as

$$\boldsymbol{u} = \sum_k \left\{\sum_{k_z}\left(\beta_{P,k,k_z}\boldsymbol{v}_{P,k,k_z} + \beta_{S,k,k_z}\boldsymbol{v}_{S,k,k_z} + \beta_{T,k,k_z}\boldsymbol{v}_{T,k,k_z}\right) + \beta_{R,k}\boldsymbol{v}_{R,k}\right\} e^{ikx}, \tag{S.11}$$

where the coefficients $\beta_{P,k,k_z}, \beta_{S,k,k_z}, \beta_{T,k,k_z}, \beta_{R,k}$ are the amplitudes of respective modes to be determined, and the mode functions read

$$\boldsymbol{v}_{P,k,k_z} = A_+^P\begin{pmatrix}1\\0\\k_z/k\end{pmatrix}e^{ik_z(z-d/2)} + A_-^P\begin{pmatrix}1\\0\\-k_z/k\end{pmatrix}e^{-ik_z(z-d/2)} + A^S\begin{pmatrix}-i(k_S/k)\sin k_S\,(z-d/2)\\0\\\cos k_S\,(z-d/2)\end{pmatrix}, \tag{S.12}$$

$$\boldsymbol{v}_{S,k,k_z} = \frac{1}{N_S}\begin{pmatrix}-(k_z/k)\cos k_z\,(z-d/2)\\0\\i\sin k_z\,(z-d/2)\end{pmatrix}, \quad \boldsymbol{v}_{R,k,k_z} = \frac{1}{N_T}\begin{pmatrix}0\\1\\0\end{pmatrix}\cos k_z\left(z - \frac{d}{2}\right), \tag{S.13}$$

$$\boldsymbol{v}_{R,k} = \frac{1}{N_R}\begin{pmatrix}\left(1-\xi_S^2\right)\left\{e^{\kappa_P(z-d/2)} - \left(1-\xi_S^2\right)e^{\kappa_S(z-d/2)}\right\}\\0\\-i\sqrt{1-\xi_P^2}\left\{\left(1-\xi_S^2\right)e^{\kappa_P(z-d/2)} - e^{\kappa_S(z-d/2)}\right\}\operatorname{sgn}(k)\end{pmatrix}. \tag{S.14}$$

We introduced the notations

$$k_S = \sqrt{\frac{c_P^2k_z^2 + \left(c_P^2 - c_S^2\right)k^2}{c_S^2}}, \quad \xi_S^2 = \frac{c_R^2}{2c_T^2}, \quad \xi_P^2 = \frac{c_R^2}{c_P^2}, \quad \kappa_{P,S} = |k|\sqrt{1 - \frac{c_R^2}{c_{P,S}^2}}, \tag{S.15}$$

and the coefficients $A_\pm^P, A^S$ for the longitudinal mode satisfy

$$c_S^2 kk_z\left(A_+^P - A_-^P\right) = \left\{c_P^2k_z^2 + \left(c_P^2 - 2c_S^2\right)k^2\right\}A^S, \tag{S.16}$$

$$c_S^2\left\{c_P^2k_z^2 + \left(c_P^2 - 2c_S^2\right)k^2\right\}\left(A_+^P + A_-^P\right) = 2\left[c_P^2\left(c_P^2 - 2c_S^2\right)k_z^2 + \left\{\left(c_P^2 - 2c_S^2\right)^2 - 2c_S^4\right\}k^2\right\}A^S. \tag{S.17}$$

We further normalise the mode functions by

$$\frac{1}{L_z}\int_{-L_z-d/2}^{d/2} dz\left|\boldsymbol{v}_\mu\right|^2 = 1, \quad \mu = (P,k,k_z), (S,k,k_z), (T,k,k_z), (R,k). \tag{S.18}$$

In the limit $L_z \to \infty$, this amounts to

$$|N_S|^2 = \frac{k^2 + k_z^2}{2k^2}, \quad |N_T|^2 = \frac{1}{2}, \quad |N_R|^2 = \frac{1}{|k|L_z}\left\{\frac{\left(1-\xi_S^2\right)^2\left(2-\xi_P^2\right)}{2\sqrt{1-\xi_P^2}} + \frac{\left(1-\xi_S^2\right)^4 + 1 - \xi_P^2}{2\sqrt{1-2\xi_S^2}} - 2\left(1-\xi_S^2\right)\frac{\left(1-\xi_S^2\right)^2 + 1 - \xi_P^2}{\sqrt{1-\xi_P^2} + \sqrt{1-2\xi_S^2}}\right\}. \tag{S.19}$$

The behaviour $|N_R|^2 \to 0$ as $L_z \to \infty$ is not unphysical: The spurious L_z dependence turns out to disappear in the final expressions for observable quantities, as demonstrated shortly. The normalisation of $\boldsymbol{v}_{P,k,k_z}$ similarly fixes $A_\pm^P, A^S$, and although they are too tedious to be written down here, they converge to constants of order unity for $L_z \to \infty$ like the other bulk modes.

Let $\epsilon^{\mu}_{ij} = \{\partial_j(\boldsymbol{v}_\mu)_i + \partial_i(\boldsymbol{v}_\mu)_j\}/2, \omega^{\mu}_{ij} = \{\partial_j(\boldsymbol{v}_\mu)_i - \partial_i(\boldsymbol{v}_\mu)_j\}/2$ be the strain and rotation tensor components of the eigenmodes labelled by $\mu = (P,k,k_z),(S,k,k_z),(T,k,k_z),(R,k)$. Substituting Eq. (S.11) into Eq. (S.8) yields

$$\boldsymbol{h}_{\text{eff}} = -\frac{\gamma/|\gamma|}{\mu_0 M_s}\sum_{\mu}\beta_\mu \begin{pmatrix} -2b_1\epsilon^{\mu}_{xx}\cos\phi\sin\phi + \left\{2b_2\epsilon^{\mu}_{xy} - (1-N_\perp)\,\omega^{\mu}_{xy}\right\}\left(\cos^2\phi - \sin^2\phi\right) \\ 2b_2\left(\epsilon^{\mu}_{zx}\cos\phi + \epsilon^{\mu}_{zy}\sin\phi\right) - N_\perp\omega^{\mu}_{zy}\sin\phi - (2N_\perp - 1)\,\omega^{\mu}_{zx}\cos\phi \end{pmatrix} e^{ikx}. \tag{S.20}$$

Now in Eq. (S.4), we are allowed to take spatial averaging in z under the thin film approximation. For wires, we also average over the wire width by integrating over x. For films, we instead decompose it into the Fourier components labelled by k. These operations eliminate all the spatial dependences (Eq. (S.7) is in fact valid only after these operations), yielding

$$\begin{pmatrix} -H_\parallel & i\omega/\mu_0|\gamma| \\ -i\omega/\mu_0|\gamma| & -H_\perp \end{pmatrix}\begin{pmatrix} n_\parallel \\ n_\perp \end{pmatrix} = -\frac{\gamma}{|\gamma|}\boldsymbol{h} + \frac{1}{\mu_0 M_s}\sum_{\mu}^{(k\text{ fixed for films})}\begin{pmatrix} a_\mu \\ b_\mu \end{pmatrix}\beta_\mu, \tag{S.21}$$

where the effective coupling constants a_μ, b_μ for each mode μ are defined by

$$a_\mu = \frac{1}{d}\int_{-d/2}^{d/2} dz\left[-2b_1\epsilon^{\mu}_{xx}\cos\phi\sin\phi + \left\{2b_2\epsilon^{\mu}_{xy} - (1-N_\perp)\,\omega^{\mu}_{xy}\right\}\left(\cos^2\phi - \sin^2\phi\right)\right] \times \begin{cases} 1 & \text{film} \\ \text{sinc}\,(kw/2) & \text{wire} \end{cases}, \tag{S.22}$$

$$b_\mu = \frac{1}{d}\int_{-d/2}^{d/2} dz\left\{2b_2\left(\epsilon^{\mu}_{zx}\cos\phi + \epsilon^{\mu}_{zy}\sin\phi\right) - N_\perp\omega^{\mu}_{zy}\sin\phi - (2N_\perp - 1)\,\omega^{\mu}_{zx}\cos\phi\right\} \times \begin{cases} 1 & \text{film} \\ \text{sinc}\,(kw/2) & \text{wire} \end{cases}. \tag{S.23}$$

Note that $a_{R,k}, b_{R,k}$ are in general larger by a factor of $\sqrt{|k|\,L_z}$ than $a_{(P,S,T),k,k_z}, b_{(P,S,T),k,k_z}$ due to the normalisation constants (S.19). This occurs due to the fact that the relative weight of the acoustic wave overlapping with the magnetic film is much greater for the surface modes than for the bulk modes. It motivates us to neglect the couplings to the bulk modes, which is ultimately justified by the results of the numerical simulations.

The mode decomposition of Eq. (S.5) is carried out by multiplying it by $\boldsymbol{v}^{\dagger}_{\mu}e^{-ikx}$ from left and integrate over the the whole volume $-L_x/2 < x < L_x/2, -L_z - d/2 < z < d/2$. Using the orthonormality of the mode functions, only the term proportional to β_μ survives on the left-hand-side. On the right-hand-side, noting $n_{\parallel,\perp}$ are nonzero only inside the region occupied by the magnet $-w/2 < x < w/2, -d/2 < z < d/2$, we obtain

$$\begin{aligned}
&\frac{1}{L_x}\int_{-L_x/2}^{L_x/2} dx\frac{1}{L_z}\int_{-L_z-d/2}^{d/2} dz\,\boldsymbol{v}^{\dagger}_{\mu}\cdot\boldsymbol{f}_{\text{eff}}e^{-ikx} \\
&= \frac{1}{L_x}\int_{-w/2}^{w/2} dx\frac{e^{-ikx}}{L_z}\int_{-d/2}^{d/2} dz\,\boldsymbol{v}^{\dagger}_{\mu}\cdot\left[\hat{\partial}_x\begin{pmatrix} -2b_1 n_\parallel\cos\phi\sin\phi \\ \left\{b_2 + \mu_0 M_s^2\,(1-N_\perp)/2\right\}n_\parallel\left(\cos^2\phi - \sin^2\phi\right) \\ \left\{b_2 - \mu_0 M_s^2\,(2N_\perp - 1)/2\right\}n_\perp\cos\phi \end{pmatrix} + \hat{\partial}_z\begin{pmatrix} \left\{b_2 + \mu_0 M_s^2\,(2N_\perp - 1)/2\right\}\cos\phi \\ \left(b_2 + \mu_0 M_s^2 N_\perp/2\right)\sin\phi \\ 0 \end{pmatrix} n_\perp\right] \\
&= -\frac{1}{L_x}\int_{-w/2}^{w/2} dx\frac{1}{L_z}\int_{-d/2}^{d/2} dz\left\{\partial_x\left(\boldsymbol{v}^{\dagger}_{\mu}e^{-ikx}\right)\right\}\cdot\begin{pmatrix} -2b_1 n_\parallel\cos\phi\sin\phi \\ \left\{b_2 + \mu_0 M_s^2\,(1-N_\perp)/2\right\}n_\parallel\left(\cos^2\phi - \sin^2\phi\right) \\ \left\{b_2 - \mu_0 M_s^2\,(2N_\perp - 1)/2\right\}n_\perp\cos\phi \end{pmatrix} \\
&\quad -\frac{1}{L_x}\int_{-w/2}^{w/2} dx\frac{1}{L_z}\int_{-d/2}^{d/2} dz\left\{\partial_z\left(\boldsymbol{v}^{\dagger}_{\mu}e^{-ikx}\right)\right\}\cdot\begin{pmatrix} \left\{b_2 + \mu_0 M_s^2\,(2N_\perp - 1)/2\right\}\cos\phi \\ \left(b_2 + \mu_0 M_s^2 N_\perp/2\right)\sin\phi \\ 0 \end{pmatrix} n_\perp \;=\; -\frac{w}{L_x}\frac{d}{L_z}\left(\overline{a_\mu}n_\parallel + \overline{b_\mu}n_\perp\right).
\end{aligned} \tag{S.24}$$

Note that in the second equality, were it not for the boundary delta functions in $\hat{\partial_{x,z}}$, we would have had additional surface terms, and consequently the result could not have been written solely in terms of a_μ, b_μ. Therefore, Eq. (S.5) reduces to

$$\rho\left(\omega^2 - \omega_\mu^2 + i\frac{\omega}{\tau}\right)\beta_\mu = -f_\mu + \frac{w}{L_x}\frac{d}{L_z}\left(\overline{a_\mu}n_\parallel + \overline{b_\mu}n_\perp\right), \quad f_\mu = \frac{1}{L_x}\int_{-L_x/2}^{L_x/2} dx\frac{1}{L_z}\int_{-d/2}^{d/2} dz\,\boldsymbol{v}^{\dagger}_{\mu}\cdot\boldsymbol{f}e^{-ikx}, \tag{S.25}$$

where the mode frequency ω_μ is given by $\omega^2_{P,k,k_z} = c_P^2\left(k^2 + k_z^2\right), \omega^2_{(S,T),k,k_z} = c_S^2\left(k^2 + k_z^2\right), \omega^2_{R,k} = c_R^2 k^2$, and the acoustic damping $1/\tau$ has been added by hand. Retaining only the surface mode and specialising in the film geometry, we derive Eq. (3) in the main text.

III. RAYLEIGH SAW AMPLITUDE

For the film geometry, by discarding the bulk acoustic waves, the problem reduces to that of one spin wave mode and one acoustic wave mode with a common wavenumber k:

$$\begin{pmatrix} n_\parallel \\ n_\perp \\ \beta_{R,k} \end{pmatrix} = -\chi_k(\omega) \begin{pmatrix} (\gamma/|\gamma|)h_k^\parallel \\ (\gamma/|\gamma|)h_k^\perp \\ f_{R,k} \end{pmatrix}, \quad \chi_k(\omega) = \begin{pmatrix} -H_\parallel + i\alpha\omega/\mu_0|\gamma| & i\omega/\mu_0|\gamma| & -a_{R,k}/\mu_0 M_s \\ -i\omega/\mu_0|\gamma| & -H_\perp + i\alpha\omega/\mu_0|\gamma| & -b_{R,k}/\mu_0 M_s \\ -d\overline{a_{R,k}}/L_z & -d\overline{b_{R,k}}/L_z & \rho\left(\omega^2 - c_R^2 k^2 + i\omega/\tau\right) \end{pmatrix}^{-1}. \tag{S.26}$$

Note that we used a different notation for the coupling constants $a_{R,k} = g_\parallel \cos\phi, b_{R,k} = g_\perp \cos\phi$ in the main text, primarily to tidy up the notations and facilitate the angular dependence analysis. We are interested in the amplitude of the Rayleigh SAW $\beta_{R,k}$ generated by some external magnetic fields $h_k^{\parallel,\perp}$ or mechanical forces $f_{R,k}$. Since the generalised susceptibility matrix is 3-by-3, it can be readily computed. We obtain

$$\begin{aligned} \det\chi_k(\omega) \begin{pmatrix} n_\parallel \\ n_\perp \\ \beta_{R,k} \end{pmatrix} &= \begin{pmatrix} \left\{(H_\perp - i\alpha\omega/\mu_0|\gamma|)\, h_k^\parallel + (i\omega/\mu_0|\gamma|)h_k^\perp\right\}\rho\left(\omega^2 - c_R^2k^2 + i\omega/\tau\right)\gamma/|\gamma| \\ \left\{(H_\parallel - i\alpha\omega/\mu_0|\gamma|)\, h_k^\perp - (i\omega/\mu_0|\gamma|)h_k^\parallel\right\}\rho\left(\omega^2 - c_R^2k^2 + i\omega/\tau\right)\gamma/|\gamma| \\ \left\{\left(1+\alpha^2\right)\omega^2/\mu_0^2\gamma^2 - H_\parallel H_\perp + i\left(H_\parallel + H_\perp\right)\alpha\omega/\mu_0|\gamma|\right\} f_{R,k} \end{pmatrix} \\ &+ \begin{pmatrix} d\left|b_{R,k}\right|^2/L_z\mu_0 M_s & -d\overline{b_{R,k}}a_{R,k}/L_z\mu_0 M_s & \frac{1}{\mu_0 M_s}\left\{\left(H_\perp - \frac{i\alpha\omega}{\mu_0|\gamma|}\right)a_{R,k} + \frac{i\omega b_{R,k}}{\mu_0|\gamma|}\right\} \\ -d\overline{a_{R,k}}b_{R,k}/L_z\mu_0 M_s & d\left|a_{R,k}\right|^2/L_z\mu_0 M_s & \frac{-1}{\mu_0 M_s}\left\{\left(H_\parallel - \frac{i\alpha\omega}{\mu_0|\gamma|}\right)b_{R,k} - \frac{i\omega}{\mu_0|\gamma|}a_{R,k}\right\} \\ \frac{d}{L_z}\left\{\left(H_\perp - \frac{i\alpha\omega}{\mu_0|\gamma|}\right)\overline{a_{R,k}} - \frac{i\omega}{\mu_0|\gamma|}\overline{b_{R,k}}\right\} & -\frac{d}{L_z}\left\{\left(H_\parallel - \frac{i\alpha\omega}{\mu_0|\gamma|}\right)\overline{b_{R,k}} - \frac{i\omega}{\mu_0|\gamma|}\overline{a_{R,k}}\right\} & 0 \end{pmatrix} \begin{pmatrix} \gamma h_k^\parallel/|\gamma| \\ \gamma h_k^\perp/|\gamma| \\ f_{R,k} \end{pmatrix}, \end{aligned} \tag{S.27}$$

where

$$\begin{aligned} \frac{1}{\det\chi_k(\omega)} &= \rho\left\{H_\parallel H_\perp - \left(1+\alpha^2\right)\frac{\omega^2}{\mu_0^2\gamma^2} - \left(H_\parallel + H_\perp\right)\frac{i\alpha\omega}{\mu_0|\gamma|}\right\}\left(\omega^2 - c_R^2k^2 + i\frac{\omega}{\tau}\right) \\ &+ \frac{d}{L_z}\frac{1}{\mu_0 M_s}\left\{\left(H_\perp - \frac{i\alpha\omega}{\mu_0|\gamma|}\right)\left|a_{R,k}\right|^2 + \left(H_\parallel - \frac{i\alpha\omega}{\mu_0|\gamma|}\right)\left|b_{R,k}\right|^2 + \frac{i\omega}{\mu_0|\gamma|}\left(\overline{a_{R,k}}b_{R,k} - \overline{b_{R,k}}a_{R,k}\right)\right\}. \end{aligned} \tag{S.28}$$

Setting $f_{R,k} = 0$ yields Eq. (6) of the main text.

In the wire geometry, the problem does not reduce to a 3-by-3 matrix inversion since the Kittel mode couples to multiple Rayleigh SAW modes with k in the range of roughly $|k| \lesssim 2\pi/w$. Nevertheless, the response of the system against a purely magnetic driving, i.e. $f_{R,k} = 0$, is still computable analytically. For this purpose, we introduce the vector notation $\boldsymbol{\beta}_R = (\beta_{R,k_1}, \beta_{R,k_2}, \cdots)^T, \boldsymbol{a}_R = (a_{R,k_1}, a_{R,k_2}, \cdots), \boldsymbol{b}_R = (b_{R,k_1}, b_{R,k_2}, \cdots)$. The linearised equations of motion (S.4), (S.5) under the mode expansion for the wire geometry are written as

$$\begin{pmatrix} n_\parallel \\ n_\perp \\ \boldsymbol{\beta}_R \end{pmatrix} = -\frac{\gamma}{|\gamma|}\begin{pmatrix} -H_\parallel + i\alpha\omega/\mu_0|\gamma| & i\omega/\mu_0|\gamma| & -\boldsymbol{a}_R/\mu_0 M_s \\ -i\omega/\mu_0|\gamma| & -H_\perp + i\alpha\omega/\mu_0|\gamma| & -\boldsymbol{b}_R/\mu_0 M_s \\ -wd\boldsymbol{a}_R^\dagger/L_xL_z & -wd\boldsymbol{b}_R^\dagger/L_xL_z & G(\omega)^{-1} \end{pmatrix}^{-1}\begin{pmatrix} h^\parallel \\ h^\perp \\ 0 \end{pmatrix}, \tag{S.29}$$

where

$$G(\omega)^{-1} = \rho\begin{pmatrix} \omega^2 - c_R^2k_1^2 + i\omega/\tau & 0 & \cdots \\ 0 & \omega^2 - c_R^2k_2^2 + i\omega/\tau & \ddots \\ \vdots & \ddots & \ddots \end{pmatrix}. \tag{S.30}$$

The inverse yields

$$\begin{pmatrix} n_\parallel \\ n_\perp \end{pmatrix} = -\frac{\gamma}{|\gamma|}\left\{\begin{pmatrix} -H_\parallel + i\alpha\omega/\mu_0|\gamma| & i\omega/\mu_0|\gamma| \\ -i\omega/\mu_0|\gamma| & -H_\perp + i\alpha\omega/\mu_0|\gamma| \end{pmatrix} - \frac{wd}{L_xL_z}\frac{1}{\mu_0 M_s}\begin{pmatrix} \boldsymbol{a}_R G(\omega)\boldsymbol{a}_R^\dagger & \boldsymbol{a}_R G(\omega)\boldsymbol{b}_R^\dagger \\ \boldsymbol{b}_R G(\omega)\boldsymbol{a}_R^\dagger & \boldsymbol{b}_R G(\omega)\boldsymbol{b}_R^\dagger \end{pmatrix}\right\}^{-1}\begin{pmatrix} h^\parallel \\ h^\perp \end{pmatrix}, \tag{S.31}$$

$$\boldsymbol{\beta}_R = -\frac{wd}{L_xL_z}G(\omega)\left(\boldsymbol{a}_R^\dagger n_\parallel + \boldsymbol{b}_R^\dagger n_\perp\right) \quad \Rightarrow \quad \beta_{R,k} = -\frac{wd}{L_xL_z}\frac{1}{\rho}\frac{\overline{a_{R,k}}n_\parallel + \overline{b_{R,k}}n_\perp}{\omega^2 - c_R^2k^2 + i\omega/\tau}. \tag{S.32}$$

Note that the second term in the curly braces in Eq. (S.31) can be considered a self-energy for the Kittel mode arising from the coupling to the Rayleigh SAWs, which can be computed by evaluating the summation over k:

$$\begin{pmatrix} \boldsymbol{a}_R G(\omega)\boldsymbol{a}_R^\dagger & \boldsymbol{a}_R G(\omega)\boldsymbol{b}_R^\dagger \\ \boldsymbol{b}_R G(\omega)\boldsymbol{a}_R^\dagger & \boldsymbol{b}_R G(\omega)\boldsymbol{b}_R^\dagger \end{pmatrix} = \frac{1}{\rho}\sum_k \frac{1}{\omega^2 - c_R^2k^2 + i\omega/\tau}\begin{pmatrix} \left|a_{R,k}\right|^2 & a_{R,k}\overline{b_{R,k}} \\ b_{R,k}\overline{a_{R,k}} & \left|b_{R,k}\right|^2 \end{pmatrix}. \tag{S.33}$$

The net effects of the self-energy are to shift the Kittel mode resonance frequency and to broaden the resonance, but only by a small amount proportional to $w/L_x \ll 1$. Note that another small factor d/L_z is compensated by the factor $|k|L_z$ arising from the normalisation constant N_R in $a_{R,k}, b_{R,k}$. Hence, we can ignore the self-energy in the leading order approximation, and obtain

$$\begin{aligned}\beta_{R,k} \approx -\frac{\gamma}{|\gamma|}\frac{wd}{L_x L_z}\left[\rho\left(\omega^2 - c_R^2 k^2 + i\omega/\tau\right)\left\{H_\parallel H_\perp - \left(1+\alpha^2\right)\frac{\omega^2}{\mu_0^2\gamma^2} - i\left(H_\parallel + H_\perp\right)\frac{\alpha\omega}{\mu_0|\gamma|}\right\}\right]^{-1} \\ \times\left[\left\{\left(H_\perp - \frac{i\alpha\omega}{\mu_0|\gamma|}\right)\overline{a_{R,k}} - \frac{i\omega}{\mu_0|\gamma|}\overline{b_{R,k}}\right\}h^\parallel + \left\{\left(H_\parallel - \frac{i\alpha\omega}{\mu_0|\gamma|}\right)\overline{b_{R,k}} + \frac{i\omega}{\mu_0|\gamma|}\overline{a_{R,k}}\right\}h^\perp\right],\end{aligned} \tag{S.34}$$

which is identical to Eq. (6) in the main text for the film geometry, apart from the appearance of the factor w/L_x in the effective coupling constants $a_{R,k}, b_{R,k}$ and the overall amplitudes.

The total displacement field $\boldsymbol{u}$ is given by the sum over k: $\boldsymbol{u} = \sum_k \beta_{R,k}\boldsymbol{v}_{R,k}e^{ikx}$. To estimate the order of magnitude of the signal, we calculate $\boldsymbol{u}$ at the surface $z = d/2$, averaged over t and x:

$$|\boldsymbol{u}|^2 = \sum_k \left|\beta_{R,k}\right|^2\left|\boldsymbol{v}_{R,k}\right|^2 = \sum_k \left|\beta_{R,k}\right|^2\frac{\left(1-\xi_S^2\right)^2 + \left(1-\xi_P^2\right)}{|N_R|^2}\xi_S^4. \tag{S.35}$$

We can again observe that the dependence on L_z drops out by L_z^{-2} coming from the prefactor in Eq. (S.34) cancelling a factor of L_z from the squares of $a_{R,k}, b_{R,k}$ and another from $|N_R|^{-2}$. For the film geometry, only one value of k resonant at ω is important. Assuming the double resonance, we have

$$\beta_{R,k} \approx -\frac{\gamma}{|\gamma|}\frac{d}{L_z}\frac{\tau}{i\rho\omega}\frac{i\mu_0|\gamma|}{\alpha\omega\left(H_\parallel + H_\perp\right)}\left\{\left(H_\perp\overline{a_{R,k}} - \frac{i\omega}{\mu_0|\gamma|}\overline{b_{R,k}}\right)h^\parallel + \left(H_\parallel\overline{b_{R,k}} + \frac{i\omega}{\mu_0|\gamma|}\overline{a_{R,k}}\right)h^\perp\right\} \approx -\frac{d}{L_z}\frac{\tau}{\rho\omega}\frac{\mu_0\gamma}{\alpha\omega}\left(\overline{a_{R,k}} - i\overline{b_{R,k}}\right)\left(h_k^\parallel + ih_k^\perp\right). \tag{S.36}$$

Plugging in the numbers $|k| = 1.5\times10^7$ rad/m, $d = 50$ nm, $\rho\omega^2 = 5\times10^{24}$ J/m^5, $\omega/\mu_0|\gamma| = 2\times10^5$ A/m, $b_1 = 3.5\times10^5$ J/m^3, $b_2 = 2b_1$, we estimate

$$|\boldsymbol{u}|^2 \sim \left(\frac{\tau\omega}{\alpha}\right)^2\times10^{-24}\times\left(\frac{\left|h^\parallel + ih^\perp\right|}{10^5\mathrm{A/m}}\right)^2\ [\mathrm{m}^2]. \tag{S.37}$$

The prefactor comes form the resonant enhancement and can be as large as $\tau\omega/\alpha > 10^6$ for YIG/GGG heterostructures. The value of $\left|h_k^\parallel + ih_k^\perp\right|$ is limited by requiring the spin wave amplitude determined by Eq. (S.27) to remain in the linear regime $\left|n_\parallel, n_\perp\right| \lesssim 10^{-2}$. For $\alpha = 10^{-3}$, we need $\left|h_k^\parallel + ih_k^\perp\right| \lesssim 1$ A/m. This leads to the attainable mean square displacement of order 10 pm. Referring to Eq. (S.21), $\beta_\mu = 1$ pm translates to an effective magnetic field of order 10^{-4} A/m, which is sufficient to trigger a secondary spin wave resonance near the detector CPW in Fig. 2(b) in the main text. Note that a similar experiment of magnetic driving and detection of acoustic waves was successfully carried out in Ref. 8 in the main text, albeit in a different geometry. Therefore, we believe the SAWs generated by spin wave resonances are also detectable in a suitably designed experimental setup.

IV. NUMERICAL SIMULATION

We perform numerical simulations of the YIG/GGG heterostructures by COMSOL Multiphysics which solves partial differential equations based on finite elements method. The geometry for the simulations is plotted in Fig. S2 where the YIG film and GGG film are separately established and simulated in a 2D model (x-z plane) and the y direction is assumed to be uniform.

The dynamics of normalised magnetisation $\boldsymbol{m} = \boldsymbol{M}/M_s = (m_x, m_y, m_z)$ and the dynamics of lattice displacement vector

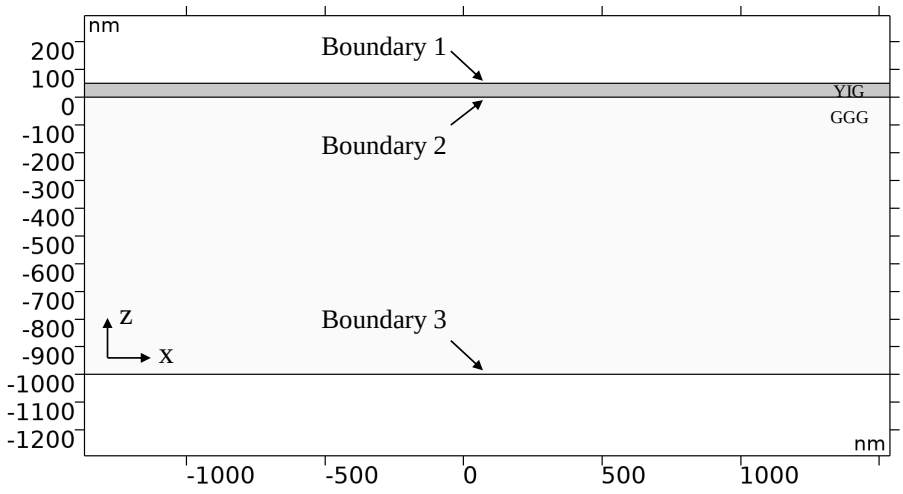

FIG. S2. Geometry of YIG/GGG heterostructures for numerical simulation. A magnetic YIG film with thickness 50mm is attached on the GGG substrate with thickness 1000mm.

$\boldsymbol{u} = (u_x, u_y, u_z)$ inside the YIG film are described by hybrid equations Eq. (S.38) with $\nabla = (\partial/\partial x, \partial/\partial z)$

$$
\begin{cases}
\dfrac{\partial m_x}{\partial t} = -\gamma(m_y H_z^{\text{eff}} - m_z H_y^{\text{eff}}) + \gamma\dfrac{2b_1}{\mu_0 M_s}\left(m_y m_z \dfrac{\partial u_z}{\partial z}\right) \\
\qquad\qquad + \gamma\dfrac{b_2}{\mu_0 M_s}\left[m_y^2\dfrac{\partial u_y}{\partial z} + m_x m_y\left(\dfrac{\partial u_z}{\partial x} + \dfrac{\partial u_x}{\partial z}\right) - m_z m_x\dfrac{\partial u_y}{\partial x} - m_z^2\dfrac{\partial u_y}{\partial z}\right], \\
\dfrac{\partial m_y}{\partial t} = -\gamma(m_z H_x^{\text{eff}} - m_x H_z^{\text{eff}}) + \gamma\dfrac{2b_1}{\mu_0 M_s}\left[m_z m_x\left(\dfrac{\partial u_x}{\partial x} - \dfrac{\partial u_z}{\partial z}\right)\right] \\
\qquad\qquad + \gamma\dfrac{b_2}{\mu_0 M_s}\left[m_y m_z\dfrac{\partial u_y}{\partial x} + m_z^2\left(\dfrac{\partial u_z}{\partial x} + \dfrac{\partial u_x}{\partial z}\right) - m_y m_x\dfrac{\partial u_y}{\partial z} - m_x^2\left(\dfrac{\partial u_z}{\partial x} + \dfrac{\partial u_x}{\partial z}\right)\right], \\
\dfrac{\partial m_z}{\partial t} = -\gamma(m_x H_y^{\text{eff}} - m_y H_x^{\text{eff}}) + \gamma\dfrac{2b_1}{\mu_0 M_s}\left[m_x m_y\left(-\dfrac{\partial u_x}{\partial x}\right)\right] \\
\qquad\qquad + \gamma\dfrac{b_2}{\mu_0 M_s}\left[m_x^2\dfrac{\partial u_y}{\partial x} + m_z m_x\dfrac{\partial u_y}{\partial z} - m_y^2\dfrac{\partial u_y}{\partial x} - m_z m_y\left(\dfrac{\partial u_z}{\partial x} + \dfrac{\partial u_x}{\partial z}\right)\right], \\
\rho_{\text{YIG}}\dfrac{\partial^2 u_x}{\partial t^2} + \eta\dfrac{\partial u_x}{\partial t} = \mu_{\text{YIG}}\nabla^2 u_x + (\lambda_{\text{YIG}} + \mu_{\text{YIG}})\left(\dfrac{\partial^2 u_x}{\partial x^2} + \dfrac{\partial^2 u_z}{\partial x \partial z}\right) + 2b_1 m_x\dfrac{\partial m_x}{\partial x} + b_2\left(\dfrac{\partial m_z}{\partial z}m_x + \dfrac{\partial m_x}{\partial z}m_z\right), \\
\rho_{\text{YIG}}\dfrac{\partial^2 u_y}{\partial t^2} + \eta\dfrac{\partial u_y}{\partial t} = \mu_{\text{YIG}}\nabla^2 u_y + b_2\left(\dfrac{\partial m_x}{\partial x}m_y + \dfrac{\partial m_y}{\partial x}m_x + \dfrac{\partial m_y}{\partial z}m_z + \dfrac{\partial m_z}{\partial z}m_y\right), \\
\rho_{\text{YIG}}\dfrac{\partial^2 u_z}{\partial t^2} + \eta\dfrac{\partial u_z}{\partial t} = \mu_{\text{YIG}}\nabla^2 u_z + (\lambda_{\text{YIG}} + \mu_{\text{YIG}})\left(\dfrac{\partial^2 u_x}{\partial z \partial x} + \dfrac{\partial^2 u_z}{\partial z^2}\right) + 2b_1 m_z\dfrac{\partial m_z}{\partial z} + b_2\left(\dfrac{\partial m_z}{\partial x}m_x + \dfrac{\partial m_x}{\partial x}m_z\right).
\end{cases}
\tag{S.38}
$$

Here the first three equations are Landau-Lifshitz-Gilbert equations in the presence of magneto-elastic coupling. The effective field $\boldsymbol{H}^{\text{eff}} = (H_x^{\text{eff}}, H_y^{\text{eff}}, H_z^{\text{eff}}) = A\nabla^2\boldsymbol{m} - M_s m_z\hat{\boldsymbol{z}} + H\cos\theta\,\hat{\boldsymbol{x}} + H\sin\theta\,\hat{\boldsymbol{y}} + \boldsymbol{h}_{\text{ext}}$ includes exchange interaction, effective hard-axis anisotropy induced by demagnetising field, static external magnetic field with in-plane angle θ and excitation field for generating spin waves. The last three equations of Eq. S.38 are the equations of motion for elastic waves, where ρ is the mass density and μ, λ are Lamé constants. The velocities of elastic waves are determined by Lamé constants with the relations $c_P = \sqrt{(2\mu + \lambda)/\rho}$ and $c_S = \sqrt{\mu/\rho}$. The damping of elastic waves is taken into account phenomenologically via the friction term $\eta\partial\boldsymbol{u}/\partial t$. Since there is no magnetisation in the GGG substrate, the dynamics of elastic waves is governed by the equations of motion without

magnetic forces

$$\begin{cases} \rho_{\mathrm{GGG}} \dfrac{\partial^2 u_x}{\partial t^2} + \eta \dfrac{\partial u_x}{\partial t} = \mu_{\mathrm{GGG}} \nabla^2 u_x + (\lambda_{\mathrm{GGG}} + \mu_{\mathrm{GGG}}) \left(\dfrac{\partial^2 u_x}{\partial x^2} + \dfrac{\partial^2 u_z}{\partial x \partial z} \right), \\ \rho_{\mathrm{GGG}} \dfrac{\partial^2 u_y}{\partial t^2} + \eta \dfrac{\partial u_y}{\partial t} = \mu_{\mathrm{GGG}} \nabla^2 u_y, \\ \rho_{\mathrm{GGG}} \dfrac{\partial^2 u_z}{\partial t^2} + \eta \dfrac{\partial u_z}{\partial t} = \mu_{\mathrm{GGG}} \nabla^2 u_z + (\lambda_{\mathrm{GGG}} + \mu_{\mathrm{GGG}}) \left(\dfrac{\partial^2 u_x}{\partial z \partial x} + \dfrac{\partial^2 u_z}{\partial z^2} \right). \end{cases} \tag{S.39}$$

Due to the presence of magnetisation inside the YIG film, extra force terms are required on the boundary 1 and 2 respectively,

$$\boldsymbol{f} = \begin{pmatrix} \mp b_2 m_x m_z \\ \mp b_2 m_y m_z \\ \mp b_1 m_z^2 \end{pmatrix}, \quad - \text{ for boundary 1 and + for boundary 2.} \tag{S.40}$$

The inclusion of these boundary forces corresponds to the delta function in Eq. (S.9) in the analytical formalism above. The free-surfacel boundary condition is applied on the top surface (boundary 1 in Fig. S2). The lattice displacement on the bottom boundary (boundary 3 in Fig. S2) is constrained with $\boldsymbol{u} = 0$. Regions $x > 1000$ nm, $x < -1000$ nm and $x < -500$ nm are manually set as high-damping regions with $\eta = 5 \times 10^{14}$ N·s/m^4 and $\alpha = 0.2$ to avoid wave reflections from the boundaries.

In the numerical simulation, we apply a magnetic field pulse at the central region of the magnetic film (width 50 nm) $\boldsymbol{h}_{\mathrm{ext}} = 10[\mathrm{mT}] \sin(2\pi f_0 t)\hat{\boldsymbol{z}}$ with duration $t = 1/f_0$ and $f_0 = 5$ GHz is the Kittel mode frequency. The elastic waves are generated due to the magneto-elastic coupling and the signals $\sqrt{u_x^2 + u_z^2}$ are extracted at the coordinates $(x, z) = (\pm 900, 0)$ nm and are integrated over time for 1ns, representing the transmission intensity. The angular dependence of transmission is plotted in Fig. S3 where the in-plane angle θ is swept from 0 to 180 degrees. It can be seen that the transmission is reciprocal when $\theta = 0$ and $\theta = \pi$, while it demonstrates maximum non-reciprocity at $\theta \sim 0.36$. The signals do not reach zero at the angles of maximum non-reciprocity presumably because of the bulk elastic waves induced by the pulse, which are neglected in the analytical calculations.

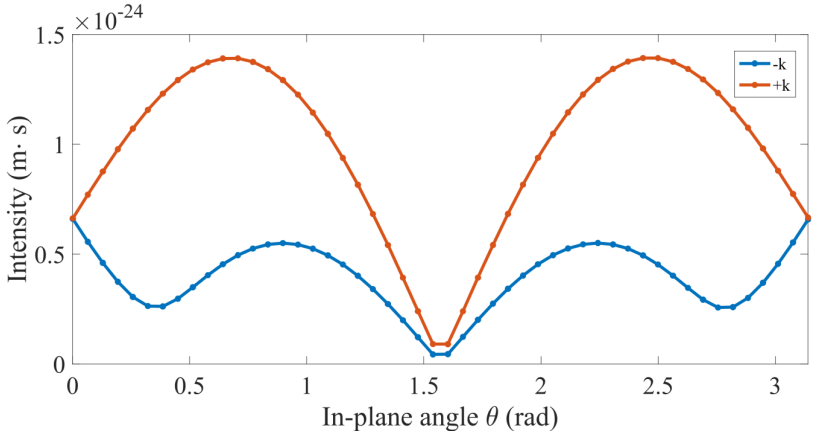

FIG. S3. Angular dependence of SAW transmission intensity integrated in time for 1 ns. The blue (red) curve is for -k (+k) case.